Seismic and Geodetic Analysis of Rupture Characteristics of the 2020 M_w 6.5 Monte Cristo Range, Nevada, Earthquake

Chengli Liu*[1], Thorne Lay[2], Fred F. Pollitz[3], Jiao Xu[4], and Xiong Xiong[1]

ABSTRACT

The largest earthquake since 1954 to strike the state of Nevada, United States, ruptured on 15 May 2020 along the Monte Cristo range of west-central Nevada. The M_w 6.5 event involved predominantly left-lateral strike-slip faulting with minor normal components on three aligned east–west-trending faults that vary in strike by 23°. The kinematic rupture process is determined by joint inversion of Global Navigation Satellite Systems displacements, Interferometric Synthetic Aperture Radar (InSAR) data, regional strong motions, and teleseismic *P* and *SH* waves, with the three-fault geometry being constrained by InSAR surface deformation observations, surface ruptures, and relocated aftershock distributions. The average rupture velocity is 1.5 km/s, with a peak slip of ∼1.6 m and a ∼20 s rupture duration. The seismic moment is 6.9×10^{18} N·m. Complex surface deformation is observed near the fault junction, with a deep near-vertical fault and a southeast-dipping fault at shallow depth on the western segment, along which normal-faulting aftershocks are observed. There is a shallow slip deficit in the Nevada ruptures, probably due to the immature fault system. The causative faults had not been previously identified and are located near the transition from the Walker Lane belt to the Basin and Range province. The east–west geometry of the system is consistent with the eastward extension of the Mina Deflection of the Walker Lane north of the White Mountains.

KEY POINTS

- Joint inversion for rupture process is performed using seismic and geodetic observations.
- The ruptures involve east–west-trending oblique left-lateral strike slip with significant normal faulting.
- The fault geometry involves two segments with strike changing by ∼23° constrained by InSAR data.

Supplemental Material

INTRODUCTION

The Walker Lane deformation belt is a 60–100 km wide zone of active faults that straddles the Nevada and California border extending from the Mojave, east of the Sierra Nevada into the Reno area and northeastern California (Fig. 1). This region lies between the Basin and Range province to the east and the Sierra Nevada block to the west, and has experienced a complex tectonic history associated with the evolution of the San Andreas fault system (e.g., Atwater, 1970) and the Great Basin (e.g., Dickinson, 2006). About 20%–23% of the present-day displacement between the Pacific and North American plates is accommodated by transpressional deformation in the Walker Lane (e.g., Thatcher *et al.*, 1999; Dixon *et al.*, 2000; Putirka and Busby, 2011; Carlson *et al.*, 2013; Bormann *et al.*, 2016). Its southern extension into the Eastern California Shear Zone has recently experienced large events such as the July 2019 Ridgecrest earthquakes (e.g., Liu, Lay, *et al.*, 2019). It is often asserted that the Walker Lane may eventually evolve into a throughgoing plate boundary transform fault (e.g., Faulds *et al.*, 2005), but it has not yet progressed far in terms of localization of deformation. The Walker Lane widens just north of the White Mountains and east of Mono Lake in a region of easterly trending faults called the Mina Deflection (Fig. 1), which extends eastward to the north–northwest-trending Petrified Springs fault (e.g., Busby, 2013; Carlson *et al.*,

1. Institute of Geophysics and Geomatics, China University of Geosciences, Wuhan, China, https://orcid.org/0000-0002-7248-6308 (XX); 2. Department of Earth and Planetary Sciences, University of California, Santa Cruz, California, U.S.A., https://orcid.org/0000-0003-2360-4213 (TL); 3. U.S. Geological Survey, Moffett Field, California, U.S.A., https://orcid.org/0000-0002-4060-2706 (FFP); 4. College of Geomatics and Geoinformation, Guilin University of Technology, Guilin, China

*Corresponding author: liuchengli@cug.edu.cn

Cite this article as Liu, C., T. Lay, F. F. Pollitz, J. Xu, and X. Xiong (2021). Seismic and Geodetic Analysis of Rupture Characteristics of the 2020 M_w 6.5 Monte Cristo Range, Nevada, Earthquake, *Bull. Seismol. Soc. Am.* **111**, 3226–3236, doi: 10.1785/0120200327

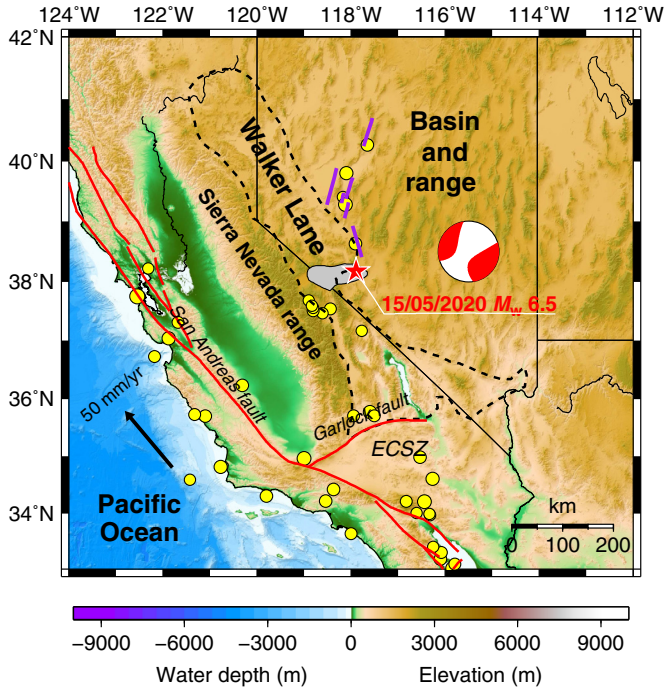

Figure 1. Tectonic structure map for the region around the 15 May 2020 M_w 6.5 Monte Cristo range, Nevada, earthquake. The event ruptured along east–west-trending strike-slip faults with left-lateral motion in the transition from the Basin and Range to the Walker Lane deformation zone along the eastern Sierra Nevada. The *W*-phase focal mechanism is shown with red regions corresponding to compressional *P*-wave motions. The red star locates the epicenter. The purple lines indicate surface ruptures of historical earthquakes to the north, mostly occurring in 1954 or earlier (Dickinson *et al.*, 2016). The yellow circles represent historic earthquakes with a magnitude larger than 6.0. The gray shaded area around the epicenter shows the location of the Mina deflection. The color version of this figure is available only in the electronic edition.

2013; Nagorsen-Rinke *et al.*, 2013; Bormann *et al.*, 2016; Busby *et al.*, 2018). Further eastward, faults in Nevada have the typical north–northeastward-trending geometry characteristic of the Basin and Range.

On 15 May 2020, a large earthquake struck within the eastern portion of the widened Walker Lane along the Mina Deflection (Fig. 1). This event (11:03:27 UTC, 38.169° N, 117.850° W, 2.7 km deep) has an M_L of 6.5. The U.S. Geological Survey National Earthquake Information Center (USGS-NEIC) *W*-phase inversion has a predominantly strike-slip moment tensor (Fig. 1), with a seismic moment of 6.77×10^{18} N · m (M_w 6.49). The moment tensor is only 68% double couple, with the best double solution having strike $\phi_1 = 73°$, dip $\delta_1 = 78°$, rake $\lambda_1 = -24°$ and $\phi_2 = 168°$, $\delta_2 = 67°$, and $\lambda_2 = -167°$. The Quick Global Centroid Moment Tensor (Global CMT) solution is similar (See Data and Resources). Either strike has a significant difference from the tectonic motion between the Pacific and North American plates (Fig. S1, available in the supplemental material to this article; Hammond and Thatcher, 2007). The event locates near the arcuate Monte Cristo range about 56 km west–northwest of Tonopah, Nevada, in a region where the USGS Quaternary faults map has no prior mapped fault. It is the largest earthquake in Nevada, because a cluster of four events to the north in 1954, which include the 16 December 1954 Fairview Peak (M_s 7.2, 39.28° N, 118.12° W) and Dixie Valley (M_s 6.8, 39.8° N 118.1° W) earthquakes, and the earlier 6 July Rainbow Mountain (M_s 6.3, 39.42° N 118.53° W) and 24 August Stillwater (M_s 7.0, 39.58° N, 118.45° W) earthquakes (e.g., Caskey *et al.*, 1996). Closer large events include an *M* 6.5 event on 30 January 1934 about 40 km to the west–northwest (38.28° N 118.36° W) and an *M* 6.8 event on 21 December 1932 about 50 km to the north (38.63° N 117.91° W). The most nearby recent event was an *M* 5.1 earthquake on 13 February 2013 (38.022° N, 118.05° W). Four aftershocks with $M \geq 5.0$ have been reported, and the Nevada Seismological Laboratory located more than 6500 aftershocks in the first two weeks after the mainshock (See Data and Resources).

Although the 15 May 2020 event caused only minor damage in the low-population source region, it is important in the context of recent activity along the Walker Lane, and in the Basin and Range. Lacking a prior identified fault (similar to the situation for the 2019 Ridgecrest earthquakes), we determine the faulting geometry and source process using seismic and geodetic information. Rather than involving typical north–northwest-striking faulting for the Walker Lane, or north–northeast-striking faulting for the Basin and Range, we find that the primary faulting involved two steeply dipping east–west-trending left-lateral strike-slip faults with a near-surface shallowly dipping normal fault along with the eastward extension of the Mina deflection.

DATA PROCESSING, FAULT MODEL PARAMETERIZATION, AND METHODOLOGY

The 2020 Monte Cristo range earthquake ground motions were well captured by geodetic and seismic observations, which provide an opportunity to perform a joint inversion for a source model with good temporal–spatial resolution. We select 30 *P* and 14 *SH* broadband teleseismic waveforms from the Incorporated Research Institutions for Seismology (IRIS) database (Fig. S2). Instrument responses are removed to obtain ground velocities and then band-pass filtered in the period range 1–300 s. We downweight the *SH* signals by a factor of 2 due to their less precise initial alignments and to balance their signal power with that of the *P* signals. Three-component waveforms for 14 strong-motion stations with epicentral distances less than 150 km are selected from the Center for Engineering Strong Motion Data (Fig. 2). Seismograms are integrated to velocity, and then band-pass filtered between 0.02 and 0.625 Hz to remove baseline drift and avoid long-period noise and deficiency of the theoretical model at higher

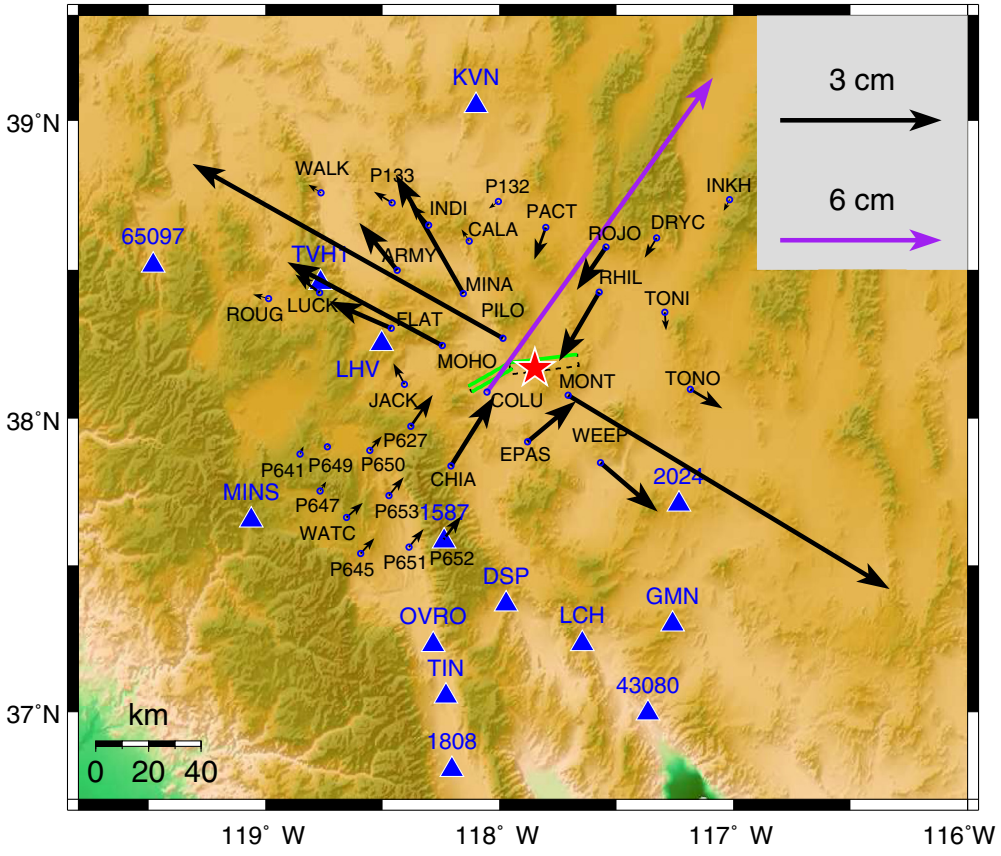

Figure 2. Map of the near-field data coverage. The red star denotes the epicenter of the mainshock. Blue triangles and circles denote the strong-motion stations and Global Navigation Satellite Systems (GNSS) sites, respectively. Black and purple arrows are GNSS coseismic observations. The green solid and black dashed outlined rectangles indicate the fault segments used in the joint inversion, with the solid side at the upper edge. The color version of this figure is available only in the electronic edition.

frequencies. All seismic waveforms are aligned on handpicked *P*- or *SH*-wave first arrivals (Liu, Lay, Xie, and Xiong, 2019).

In addition, we select coseismic Global Navigation Satellite Systems (GNSS) static displacements at 35 sites (Fig. 2) from Hammond *et al.* (2021), for which detailed information is shown in Table S1. The Interferometric Synthetic Aperture Radar (InSAR) line of sight (LoS) observations for two acquisitions of the Sentinel-1A/B satellites operated by the European Space Agency are calculated using the GMTSAR software (Sandwell *et al.*, 2016) (Fig. 3; see supplement text for processing details). The ascending and descending interferograms are both from Synthetic Aperture Radar (SAR) acquisitions on 11 and 17 May 2020, so postseismic deformation in the first two days after the event could contribute to the signals.

The 2020 Nevada earthquake lacked a previously mapped Quaternary fault, so the mechanism has to be specified by other observations. The *W*-phase moment tensor has a substantial non-double-couple component, raising questions about whether the best-double couple geometry is appropriate for the modeling. The earthquake produced low-amplitude slip on ~east–northeast-trending surface ruptures parallel to the overall trend of the aftershocks (Fig. 4a), as well as secondary cracking on north–south structures (e.g., Elliott *et al.*, 2020; Koehler *et al.*, 2021). To derive a rupture model for the mainshock, we constrain the fault geometry based on trends in the InSAR observations, surface ruptures investigated by Koehler *et al.* (2021), and relocated aftershocks from Ruhl *et al.* (2021) (locations in Fig. 4a and moment tensor solutions in Fig. 4b), which generally favor the east–west (~73° strike)-trending nodal plane in the moment tensor best double-couple solution. Ascending and descending tracks of Sentinel-1A/B covered the full extent of the 2020 rupture, offering excellent resolution of the surface displacement field around the rupture, as seen in Figure 3, with little surface rupture being evident.

Given the well-defined surface displacement, an accurate mainshock hypocenter is essential for determining the dipping direction of the fault. We adopted the relocated hypocenter from Ruhl *et al.* (2021) and conducted a series of preliminary finite-fault inversions, considering single- and multiple-segment models to specify the mainshock fault geometries. The Global Positioning System (GPS) and seismic data could be well fit using two-fault models similar to the model of Zheng *et al.* (2020), which involves uniform dip on the western fault plane. However, the InSAR data considered in the present study indicate more complexity near the fault intersection that prompt us to include variable dip in the western section. Based on these trial inversions, we propose a faulting model with three rupture segments. Two fault segments labeled F1 (eastern fault) and F2 (western shallow fault) have strikes of 83° and 60°, respectively (Fig. 4b). Their upper edges track along the surface ruptures (mainly in the west), and their dips of 78° and 60° to the southeast, respectively, are consistent with the relocated aftershock distribution (Ruhl *et al.*, 2021) and the *W*-phase moment tensor solution (Fig. 4c,d). The hypocenter is assumed to be on F1 with a slight adjustment (117.885° W, 38.188° N, 3.8 km) to

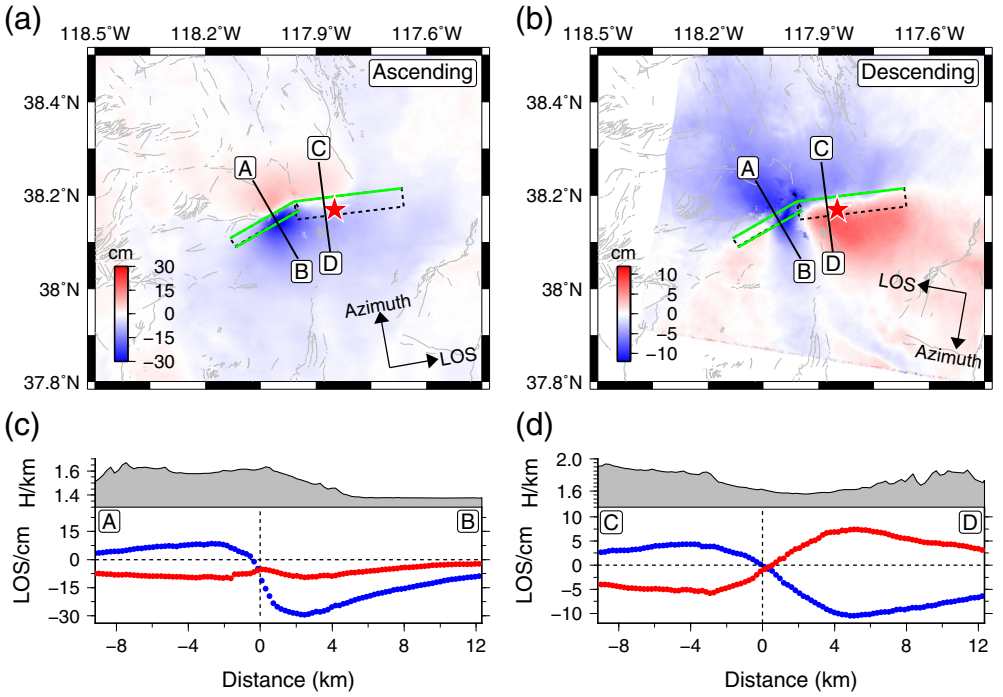

Figure 3. Unwrapped Interferometric Synthetic Aperture Radar (InSAR) line of sight (LoS) displacement image of (a) ascending and (b) descending tracks, with both having postearthquake acquisitions on 17 May 2020. Red colors (positive) show movement of the ground toward the satellite, and blue colors (negative) show movement of the ground away from the satellite. (c) and (d) show profiles of LoS deformation along lines AB and CD, respectively, which are perpendicular to the local strike of the two segments. Blue and red dots represent surface LoS displacement for ascending and descending data, respectively. The green solid and black dashed outlined rectangles indicate the fault segments used in the joint inversion, with the solid side at the upper edge. The color version of this figure is available only in the electronic edition.

provide consistency with the InSAR observations and surface ruptures. In the western section, we also place a near-vertical fault segment (labeled F3) at depths greater than 5 km with the same strike as F2 to fit the seismicity. We subdivide these three fault segments into 277 subfaults with dimensions of 2.0 km × 1.65 km. The detailed fault parameters are listed in Table S3.

We use a simulated annealing algorithm in the wavelet domain to obtain the best-fitting model for the geodetic data and seismograms (Ji *et al.*, 2002, 2003). The finite-fault inversion method solves for slip amplitude, rake angle, and rupture initiation time simultaneously. In this study, we allow both the rise and fall times of the asymmetric slip rate function for each subfault to vary from 0.2 to 1.6 s. The corresponding rupture duration for each subfault is thus limited between 0.4 and 3.2 s. We let the slip amplitude vary from 0.0 to 2.0 m, and the rake angle is constrained from −74° to 46°, straddling the *W*-phase solution value (−24°). The rupture velocity is allowed to vary from 0.5 to 3.5 km/s. The rupture is allowed to progress smoothly across the two subfaults without imposed delay. Green's functions for both the static displacements and seismic datasets are computed using a 1D layered velocity model (Mangino *et al.*, 1993; Fig. S3).

Generally, joint inversion always presents the challenge of reconciling the fitting of distinct datasets by coseismic finite-fault inversion, especially for InSAR observations, which may include postseismic deformation contributions such as early afterslip, aftershocks, and viscoelastic relaxation, rather than a purely coseismic slip (e.g., Yano *et al.*, 2014). There is a detectable postseismic deformation over several months within 70 km of the epicenter in the geodetic observations (Hammond *et al.*, 2021). Hammond *et al.* (2021) analyzed the MAGNET stations occupied quickly after the mainshock, finding negligible displacement uncertainty within the first 10 days after the 2020 mainshock. MAGNET was originally designed to supplement geographic coverage of the regional, high-precision, continuous Global Navigation Satellite Systems Networks (Blewitt *et al.*, 2009). The acquisition of the first postevent SAR images is only two days after the mainshock. So, we can focus on the effectively coseismic kinematic rupture of the mainshock by joint inversion of GNSS static displacements, seismic waveforms, and the ascending and descending tracks of Sentinel-1A/B to determine the coseismic source process for our undoubtedly simplified fault model parameterization.

In the joint inversion, the overall weight of the static displacements is chosen to be equal to the weight of the seismic waveforms. However, the InSAR and GNSS statics have different data density; although we downsample the InSAR data, their number is still far greater than that of the GNSS observations. We, therefore, need to specify the relative weight assigned to the two types of static data. The relative weight is determined by trial and error. We conducted a range of inversions weights and found that a 10:1 weight of GNSS statics versus InSAR data produced a relatively small residual for all geodetic observations.

CHECKERBOARD TEST

Checkerboard tests are commonly used to explore data resolution and inversion stability. We conduct a checkerboard test to evaluate temporal and spatial resolution provided by the

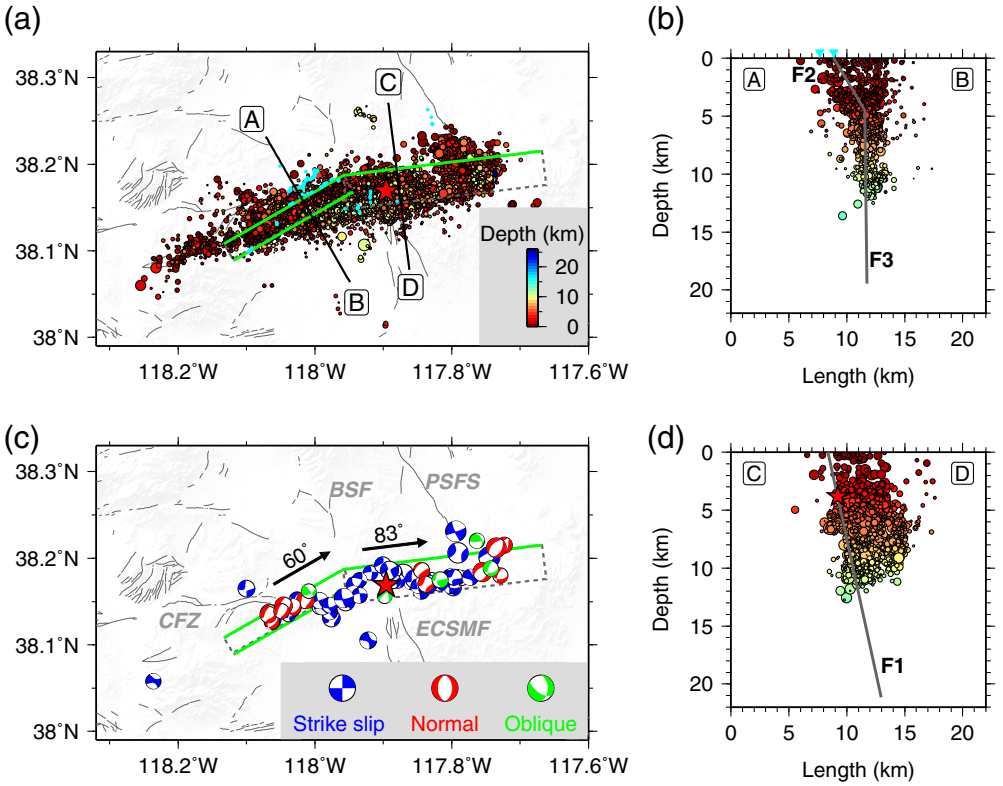

Figure 4. The distribution of aftershocks 108 days after the mainshock. (a) Relocated aftershocks from Ruhl *et al.* (2021). Circles are scaled relative to the magnitude and color coded by depth. Gray lines are fault traces from the U.S. Geological Survey (USGS) Quaternary Fault and Fold Database. Gray dashed rectangles with solid green lines show the fault geometry. Cyan dots are the mapped traces of surface rupture (Koehler *et al.*, 2021). (b) *W*-phase and regional moment tensor solutions from the USGS-National Earthquake Information Center (NEIC) for events with magnitude ≥ 3.0. Different colors represent different source mechanism categories indicated by the inset. (c) and (d) show the cross section of aftershock distribution along profiles AB and CD shown in (a). The cyan inverted triangles show the surface ruptures, and the thick gray lines are the inferred fault segments. BSF, Benton Springs fault; CFZ, Candelaria fault zone; ECSMF, eastern Columbus Salt Marsh fault; PSFS, Petrified Springs fault system. The color version of this figure is available only in the electronic edition.

joint inversion. We construct a theoretical model with slip patches of 6 km × 4.95 km (3 × 3 subfaults) (Fig. S4) for our faulting configuration to generate synthetic datasets. Synthetics for all four data sets are generated with the same Green's functions used in the actual inversion. Adopting the same inversion procedure and weighting as used for the actual data, we jointly inverted the synthetic datasets, resulting in the distribution of faulting parameters shown in Figure S5, displaying good resolution in the shallow parts of the model. The resolution analysis indicates that the main slip pattern that we obtain below represents well-resolved features over scales of about ~5 km in the upper 10 km along the rupture zone.

INVERSION RESULTS

The inverted coseismic slip model, along with the corresponding distributions of subfault rise time, slip rate, and moment-rate functions, is shown in Figure 5. The inversion results show that the rupture initiated at a depth of 3.8 km on F1 and then propagated bilaterally along strike, releasing a cumulative moment of 6.9×10^{18} N · m, corresponding to a moment magnitude M_w 6.5. The centroid depth is 10.7 km, which is comparable with the USGS-NEIC *W*-phase solution (11.5 km). The slip distribution is not uniform. Most of the slip during the mainshock is located along F1, and spans depths between 2 and 16 km, and there is minor near-surface slip in the eastern part of F1. There is no significant near-surface slip on F2 (Fig. 5a), and F3 dominates the western slip. The dominance of slip on F1 and F3 accounts for the success of two-fault models for matching the GNSS and seismic observations. The InSAR data limit the amount of near-surface slip and resolves extensional faulting on F2. The rupture has an average rupture velocity of ~1.5 km/s, and the peak slip value is ~1.6 m. Aftershocks tend to lie outside of large-slip areas for the coseismic model (Figs. 5a and 6), but there is some overlap, especially on F3, which may be associated with residual stresses from the coseismic process or activation of off-fault seismicity (Fig. 4c). The aftershock focal mechanisms in Figure 4b indicate that normal faulting is distributed along the western segment, consistent with primarily normal-faulting slip on F2. Slightly oblique strike-slip faulting aftershocks concentrate near the intersections of the three faults and along eastern segment F2.

Depth-dependent rise time variation is indicated in the rupture model; the average rise time for the shallower asperities (<5 km deep) is about 0.5 s longer than for the deeper slip (Fig. 5b), yielding a corresponding slower slip rate (Fig. 5c). The average rise time and slip rate are 1.7 s and 0.4 m/s, respectively. The entire coseismic rupture process lasted at least 20 s, with minor, poorly resolved slip possibly persisting to 25 s (Fig. 5d); over 90% of the slip occurred within the first 13 s. The late moment release is associated with minor slip on the down-dip portion of the faults and may be a modeling artifact. The equivalent moment tensor of the three-fault model has significant non-double-couple component (Fig. 5d), which

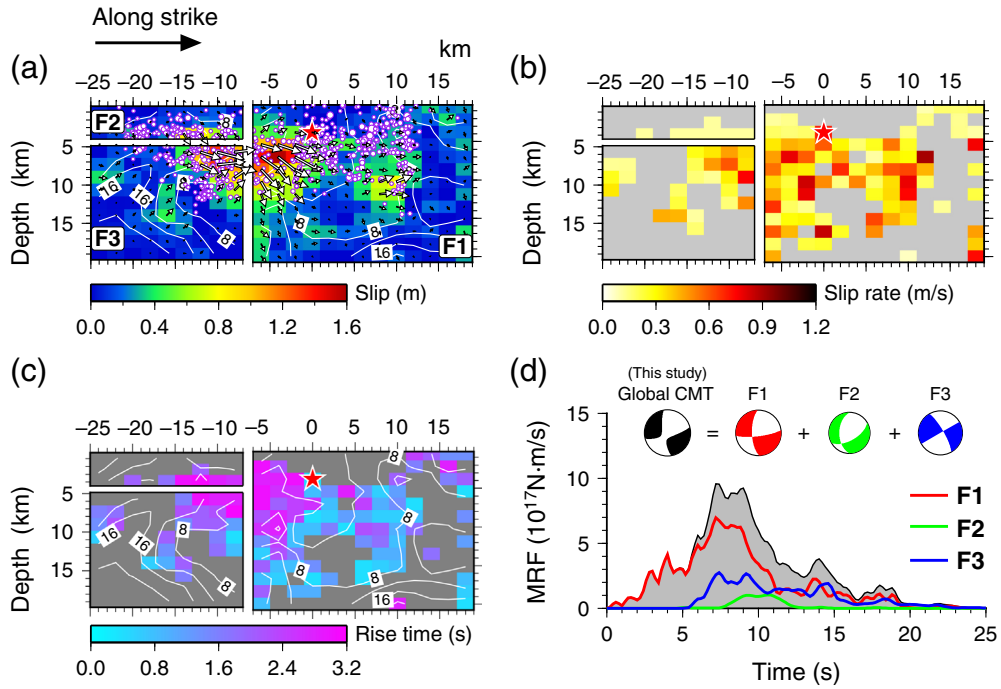

Figure 5. Preferred joint inversion results for the 15 May 2020 Nevada earthquake. (a) The inverted slip distribution on three fault segments, the fault parameters are shown in Table S2. The red star locates the hypocenter on F1. White contours indicate the rupture initiation time in seconds. White arrows indicate the direction and amplitude of slip of the hanging wall relative to the footwall. The color bar shows the slip amplitude scale. White dots with a purple edge indicate aftershocks with magnitude ≥ 2.5. (b) and (c) are the distribution of rise time and slip rate of the rupture model, respectively; subfaults with slip magnitude less than 0.2 m are excluded. Slip rate is defined as the ratio of fault slip to rise time. (d) The moment rate function for the slip model. Three contributions from the three fault segments are shown by colored curves, and the gray-shaded region indicates the total moment rate. The color version of this figure is available only in the electronic edition.

is very similar to the *W*-phase solution from USGS (Fig. 1). The moment tensor solution of each fault segment varies greatly (Fig. 5d), indicating complex fault geometry and rupture processes.

The kinematic rupture expansion is depicted with intervals of 2 s in Figure 6, indicating a complex source process. The snapshots show that the rupture propagated down-dip on F1 in the first 4 s with a rupture velocity less than 1.5 km/s, and there is no resolved rupture of F2 and F3 in the early stage. After 6 s, the rupture rapidly expanded bilaterally with a rupture velocity of >2.0 km/s, with significant slip on F3 and minor slip on F2, which does not reach the surface. The seismic moment rate peaks around 7 s, and then begins to decrease gradually (Figs. 5d and 6). The complexity of the source process reflects the heterogeneous properties along the fault zone, which is usually characterized by barriers or asperities. Referring to the checkerboard test results in Figure S5, we expect degraded resolution of the faulting parameters at depths greater than 10 km.

The broadband radiated seismic energy reported by IRIS (See Data and Resources) is $E_R = 1.4 \times 10^{14}$ J for a 50 s interval, using the procedure of Convers and Newman (2011). Using our estimate of seismic moment M_0, we obtain a moment-scaled radiated energy value of $E_R/M_0 = 2.0 \times 10^{-5}$. This value is about twice as large as measured for the 2019 Ridgecrest foreshock and mainshock (Liu, Lay, *et al.*, 2019).

The seismic waveforms and static displacements fit for this three-fault kinematic model are shown in Figures 7–9 and Figure S6. The fitting error for each data set is shown in Table S4. The model explains well the teleseismic waveforms (Fig. S6) and the most strong-motion observations (Fig. 8), although large mismatches can be seen for several strong-motion stations containing higher-frequency signals (e.g., OVRO, TIN, and LHV). These misfits are presumably due to 3D basin effects that cannot be well modeled using a 1D crustal velocity model. Static GNSS displacements (Fig. 7) fit very well in our joint inversion. Overall, this coseismic slip model provides good fits to the various datasets (Table S4), suggesting that the rupture model is a reasonable representation of the source process.

DISCUSSION

Inversion of the seismic and geodetic static data set for the simple three-fault model achieves good predictions of the data. The overall faulting characteristics are compatible with single-fault inversion (Hammond *et al.*, 2021) and two-fault inversion (Zheng *et al.*, 2020). Nevertheless, aftershock relocations indicate that the aftershock zone comprises many distinct fault structures with various orientations (Ruhl *et al.*, 2021). In addition to the three main fault segments that we constructed, one of the most apparent west-dipping trends in the aftershocks locates along a north-striking extension of the eastern Columbus Salt Marsh fault west of the mainshock hypocenter (Ruhl *et al.*, 2021). To explore the possible existence of slip on such a west-dipping structure, we parameterized a four-fault joint inversion by adding a new fault segment (F4) that extends across the three-fault model at the fault intersection, dipping to the west at 70° (Fig. S7). The four-fault model can also account for the geodetic displacements and seismic waveforms with a small additional reduction in misfit (Figures S8–S11), but the evidence for the north–south fault being activated is marginal.

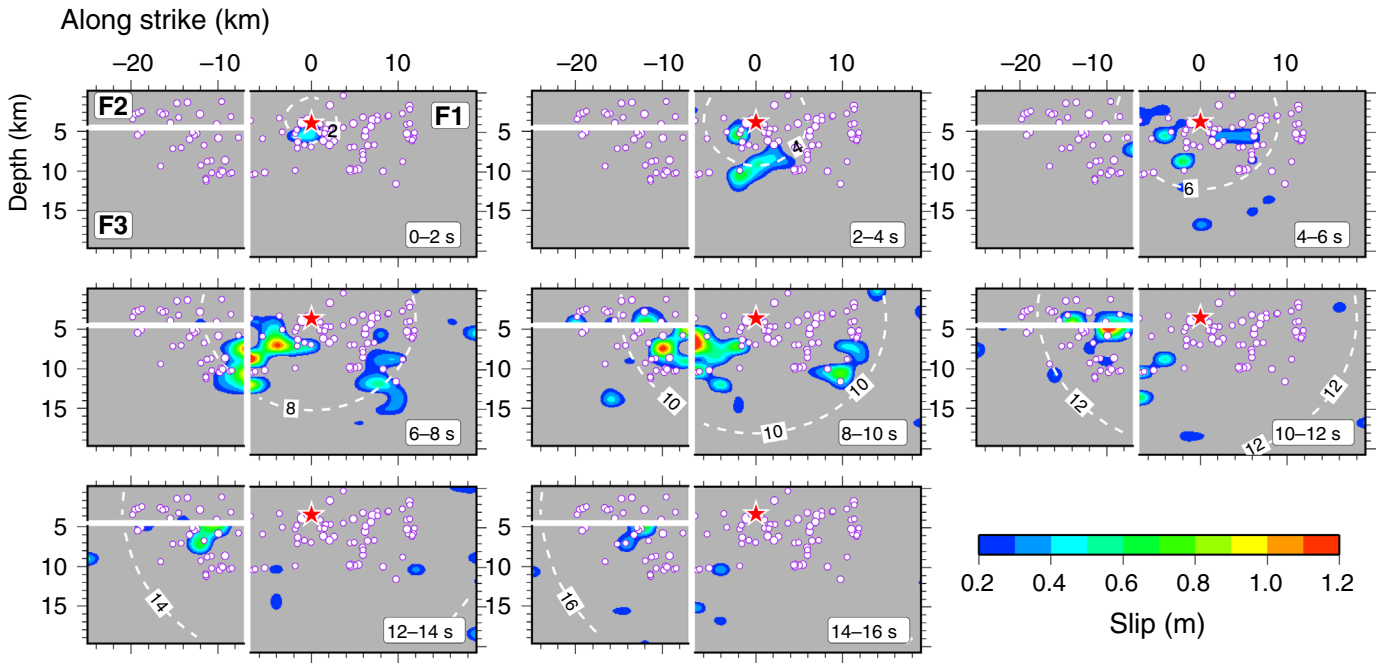

Figure 6. Rupture snapshots for the joint inversion model in Figure 5a with a timestep of 2 s. The color indicates the fault slip. The white dashed contour denotes the pseudorupture front for a rupture velocity of 1.5 km/s. We do not have confidence in minor slip and the moment rate function after 16 s (Fig. 5d), and slip less than 0.2 m is excluded. The color version of this figure is available only in the electronic edition.

So, the three-fault model presented here is our preferred coseismic rupture model.

The segmented rupture of the 2020 Monte Cristo range earthquake, the lack of prior mapped Quaternary faulting, and the presence of minor irregular surface break all suggest a relatively immature fault system that has not accumulated significant total slip. Liu, Lay, *et al.* (2019) argued that the 2019 M_w 7.1 Ridgecrest earthquake also ruptured an immature fault zone with a low-rupture velocity. The Monte Cristo range faulting does not appear to involve as many fault segments and has higher moment-scaled radiated energy, so it is perhaps somewhat less complex of a rupture, but the rupture does appear to have been influenced by the fault segmentation. The faulting geometry is more clearly aligned with the Mina deflection than with any of the northerly trending fault systems in the Walker Lane and the Basin and Range, so it is reasonable to infer that the activated faulting is associated with the widened portion of the Walker Lane. Given the lack of localization of the north–northwest strike-slip faulting in the Walker Lane overall, the activation of sinistral and normal faulting in the Mina deflection (e.g., Nagorsen-Rinke *et al.*, 2013) that is apparently connected to this event can be expected to continue.

The inverted slip distribution for the 2020 Monte Cristo range event suggests a moderate shallow coseismic slip deficit, especially along eastern segment F1. It is essential to consider how the coseismic slip amplitude varies with depth. Previous studies have indicated that slip in the middle of the

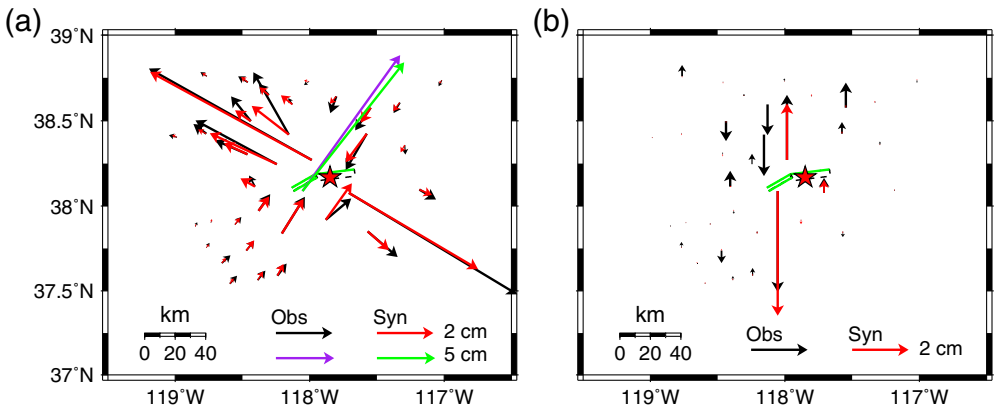

Figure 7. Comparison between the observed and synthetic GNSS coseismic displacements of the 2020 Nevada earthquake for the finite-fault inversion with three fault segments in Figure 5a. (a) The data (black and purple) and synthetic (red and green) horizontal GNSS components. (b) The vertical GNSS component data (black) and synthetics (red). The green solid and black dashed rectangles indicate the assumed fault segments, with the shallow (surface) edge having solid lines. The color version of this figure is available only in the electronic edition.

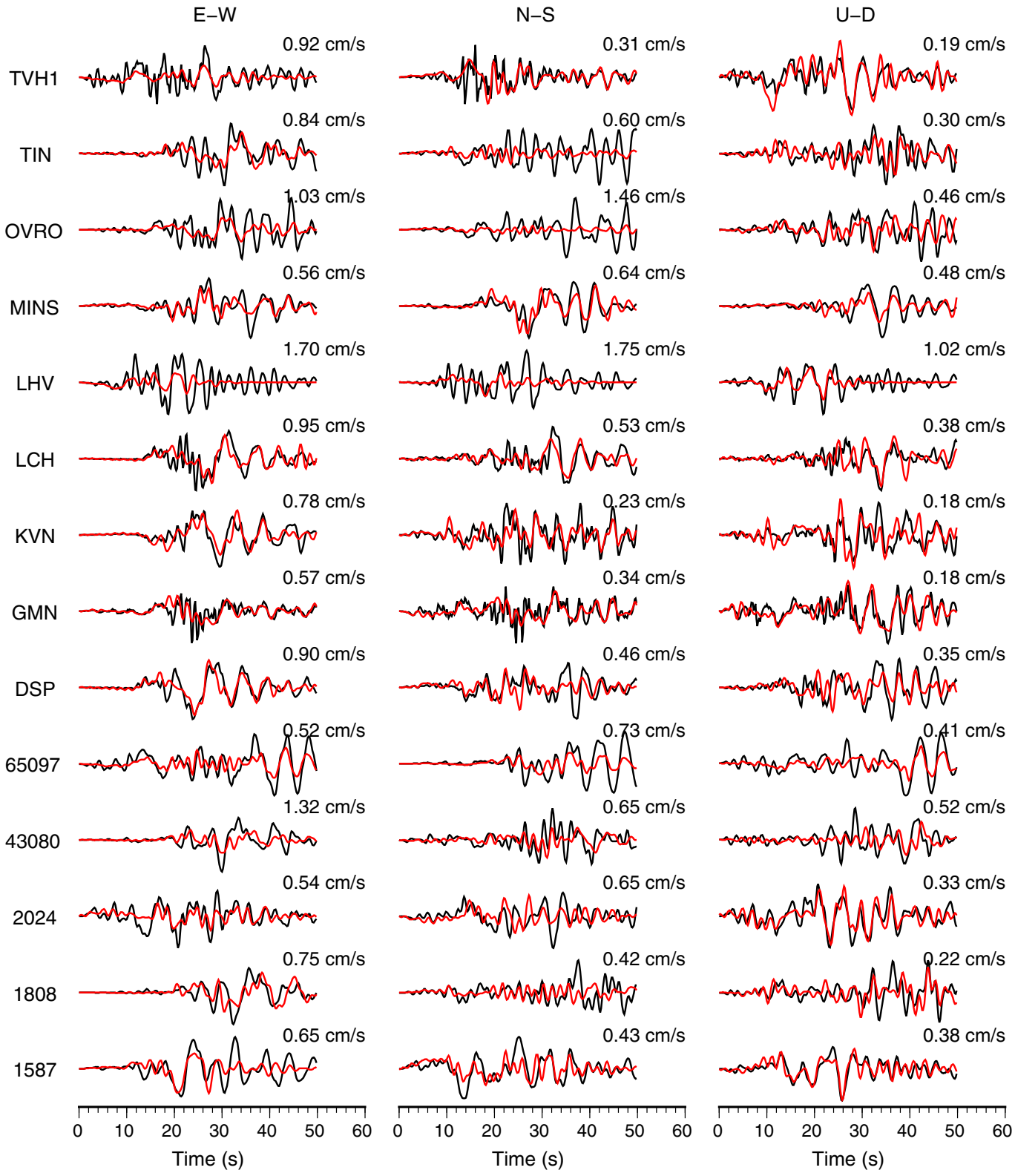

Figure 8. Comparison of observed three-component strong-motion records (black lines) and synthetic seismograms (red lines) for the slip model in Figure 5a with three fault segments. Both data and synthetics are manually aligned in the inversion on the first *P* arrivals as shown and band-pass filtered between 0.02 and 0.625 Hz. The station name is indicated on the left; the number at the top right of each trace is the maximum velocity of the observed signals in centimeters per second. The color version of this figure is available only in the electronic edition.

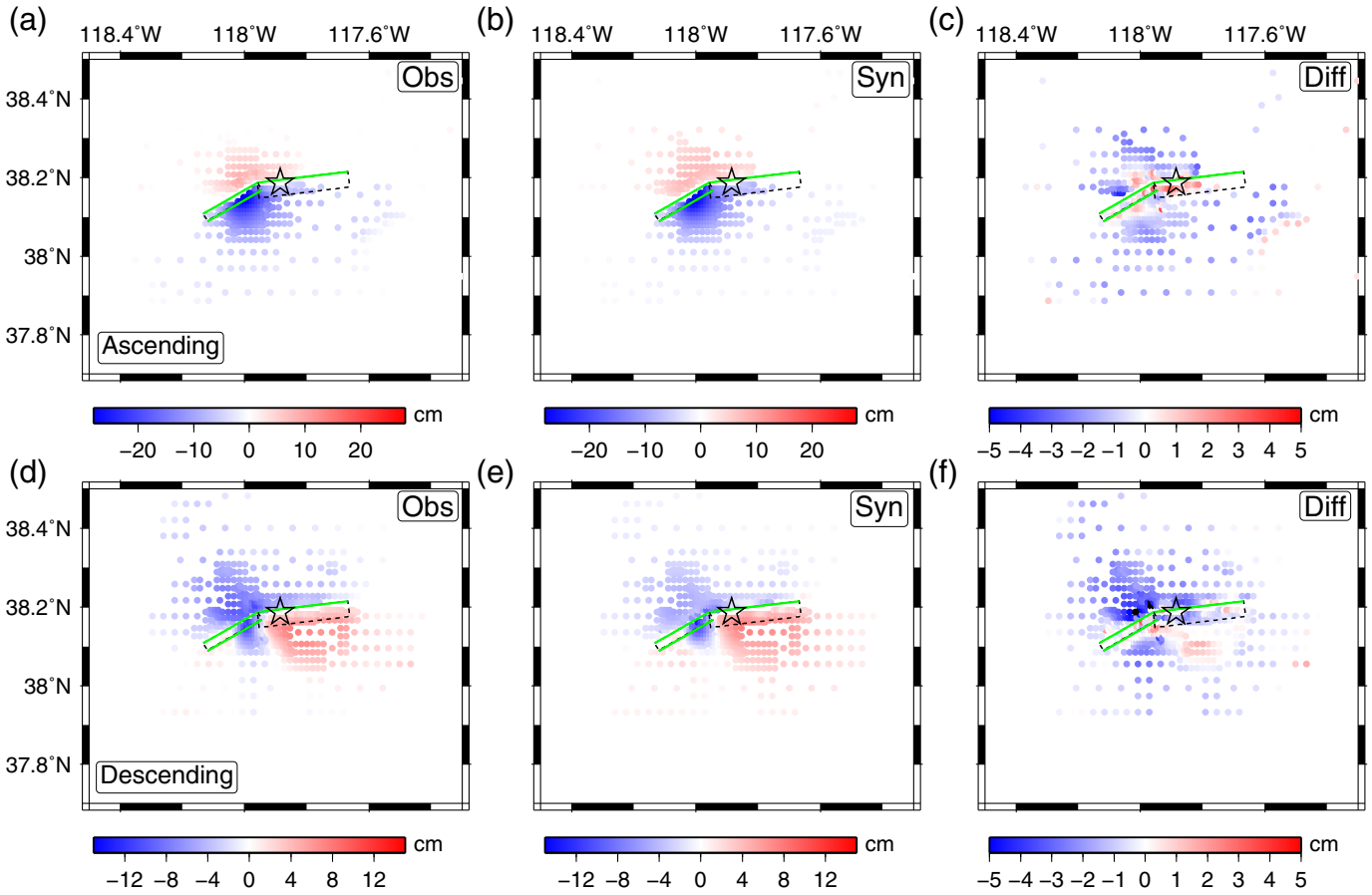

Figure 9. LoS displacement fields and synthetics. (a) and (d) LoS displacements for the ascending and descending Sentinel-1, respectively. (b) and (e) Prediction of LoS displacements from the joint seismic-GNSS inversion model in Figure 5. (c) and (f) Residuals of LoS displacements along the ascending and descending path, respectively. Note the difference in color scale. Red (positive) indicates movement of the ground toward the satellite, and blue (negative) indicates movement of the ground away from the satellite. The rectangles show the fault plane, and the star is the epicenter of the mainshock. The green solid and black dashed outlined rectangles indicate the fault segments used in the joint inversion, with the solid side at the upper edge. The vertical F3 plane is not distinguishable from the lower edge of F2 in the subfigures. The color version of this figure is available only in the electronic edition.

seismogenic layer systematically exceeds slip at the surface for many strike-slip events (Fig. 10). The maximum along-strike average slip of the Nevada earthquake occurred in the depth interval between 6 and 9 km, comparable with the 2020 M_w 6.7 Elazığ Turkey event (Xu *et al.*, 2020), but deeper than for several other strike-slip earthquakes in the Eastern California Shear Zone (Fig. 10). The variation in shallow slip deficit might be attributed to different seismogenic depths or different degrees of fault maturity among strike-slip events. Given that the crustal strength decreases toward the surface, the rupture termination in the uppermost crust indicates either negligible preseismic elastic strain accumulation, abundant velocity strengthening material in the top few kilometers, or a combination of both. Several large strike-slip earthquakes have not been found to have shallow slip deficit, such as the 2010 M_w 6.9 Yushu earthquake and the 2018 M_w 7.5 Palu earthquake, which ruptured the entire seismogenic layer to the surface (e.g., Zhang *et al.*, 2013; Socquet *et al.*, 2019). However, the significant shallow afterslip along the western section for the 2020 Nevada event (fig. 5 of Hammond *et al.*, 2021) indicates that the coseismic slip deficit will be partially accommodated by the aseismic slip in the uppermost crust.

CONCLUSIONS

Joint inversion of geodetic and seismic observations indicates that the 15 May 2020 Monte Cristo range M_w 6.5 earthquake ruptured with left-lateral and minor normal faulting on three easterly trending steeply dipping faults in the eastern Walker Lane along the extrapolation of the Mina deflection into western Nevada. The earthquake involved slow rupture expansion that spread from the eastern fault segment with strike 83° to down-dip slip on the western fault segment with strike 60°. InSAR surface displacements provide tight constraints on the 23° change in strike of the segments. Slip of up to 1.6 m occurred in the main slip patch from 2 to 16 km depth on the eastern fault, with several decimeters of shallow slip at its eastern extremity, and with no significant slip in the upper 5 km located on the western fault. There is a shallow coseismic

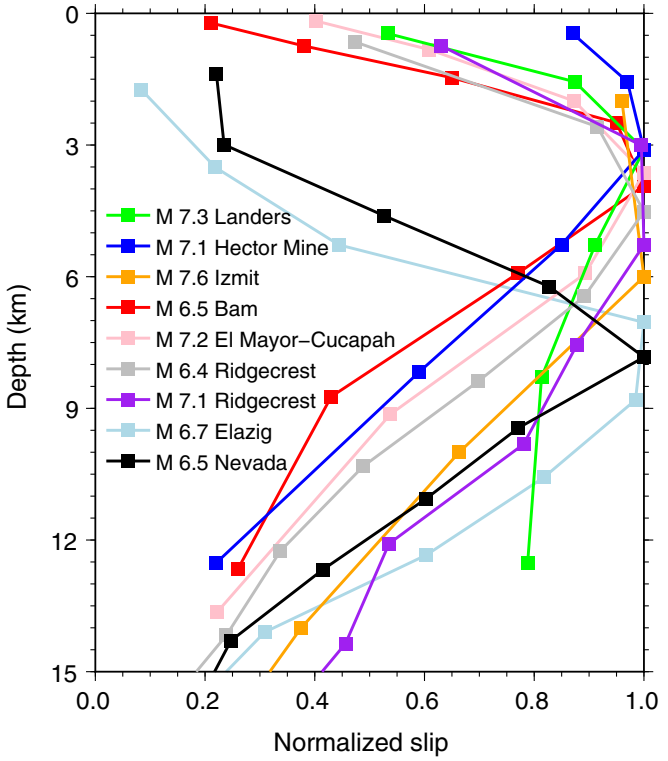

Figure 10. Along-strike averaged coseismic slip as a function of depth for the M_w 6.5 Nevada earthquake (solid black line), as well as for several other strike-slip earthquakes (Liu, Lay, *et al.*, 2019; Jin and Fialko, 2020; Xu *et al.*, 2020). The color version of this figure is available only in the electronic edition.

slip deficit overall, notably near the hypocenter on the eastern fault. Aftershocks are concentrated near the slip zone, with some in close proximity to the large-slip patches in the east.

DATA AND RESOURCES

Teleseismic body-wave recordings were obtained from the Incorporated Research Institutions for Seismology (IRIS) data center available at http://ds.iris.edu/wilber3/find_event (last accessed August 2020). Strong-motion recordings were collected from https://strongmotioncenter.org/ (last accessed August 2020). The Quick Global Centroid Moment Tensor (Global CMT) solution is available at https://www.globalcmt.org/CMTsearch.html (last accessed October 2020). The estimated far-field broadband radiated elastic energy was reported at IRIS, which is available at http://ds.iris.edu/spud/eqenergy/18152286 (last accessed October 2020). The Global Positioning System (GPS) coseismic data are from Hammond *et al.* (2021). The Network of the Americas (NOTA) GPS data wave originated with the Geodetic Facility for the Advancement of Geoscience (GAGE) Facility, operated by UNAVCO, Inc., with support from the National Science Foundation (NSF) and the National Aeronautics and Space Administration (NASA) under NSF Cooperative Agreement EAR-1724794. GPS data were originally provided from the University of Nevada Geodetic Laboratory (http://geodesy.unr.edu/, last accessed June 2021), following the processing described in Blewitt *et al.* (2018). All figures were generated using the open-source Generic Mapping Tools software (Wessel and Smith 1991). The supplemental material includes two texts, 12 figures, and four tables to support the main article.

DECLARATION OF COMPETING INTERESTS

The authors acknowledge that there are no conflicts of interest recorded.

ACKNOWLEDGMENTS

The authors thank associate editor Ronni Grapenthin, editor Thomas Pratt, and two anonymous reviewers for helpful comments on the article. This article benefited from useful commentary from Kathryn Materna and Evelyn Roeloffs at the U.S. Geological Survey (USGS). The authors thank Yuri Fialko at University of California (UC) San Diego for providing coseismic slip data of several other strike-slip earthquakes. C. Liu was supported by National Natural Science Foundation of China (Grant Number 41974056). T. Lay's research on earthquakes is supported by the U.S. National Science Foundation (NSF) Grant Number EAR1802364.

REFERENCES

Atwater, T. (1970). Implications of plate tectonics for the Cenozoic tectonic evolution of western North America, *Geol. Soc. Am. Bull.* **81,** 3513–3536, doi: 10.1130/0016-7606(1970)81[3513:IOPTFT]2.0.CO;2.

Blewitt, G., W. C. Hammond, and C. Kreemer (2018). Harnessing the GPS data explosion for interdisciplinary science, *Eos* **99,** doi: 10.1029/2018EO104623.

Blewitt, G., C. Kreemer, and W. C. Hammond (2009). Geodetic observation of contemporary deformation in the northern Walker Lane: 1. Semipermanent GPS strategy, in *Late Cenozoic Structure and Evolution of the Great Basin–Sierra Nevada Transition*, J. S. Oldow and P. H. Cashman (Editors), Geological Society of America, Special Paper 447, 1–15, doi: 10.1130/2009.2447(01).

Bormann, J. M., W. C. Hammond, C. Kreemer, and G. Blewitt (2016). Accommodation of missing shear strain in the Central Walker Lane, western North America: Constraints from dense GPS measurements, *Earth Planet. Sci. Lett.* **440,** 169–177, doi: 10.1016/j.epsl.2016.01.015.

Busby, C. J. (2013). Birth of a plate boundary at ca. 12 Ma in the Ancestral Cascades Arc, Walker Lane belt of California and Nevada, *Geosphere* **9,** 1147–1160, doi: 10.1130/GES00928.1.

Busby, C. J., K. Putirka, B. Melosh, P. R. Renne, J. C. Hagan, M. Gambs, and C. Wesoloski (2018). A tale of two Walker Lane pull-apart basins in the ancestral Cascades arc, Central Sierra Nevada, California, *Geosphere* **14,** 2068–2117, doi: 10.1130/GES01398.1.

Carlson, C. W., C. J. Pluhar, J. M. G. Glen, and M. J. Farner (2013). Kinematics of the west-central Walker Lane: Spatially and temporally variable rotations evident in the Late Miocene Stanislaus group, *Geosphere* **9,** 1530–1551, doi: 10.1130/GES00955.1.

Caskey, S. J., S. G. Wesnousky, P. Zhang, and D. B. Slemmons (1996). Surface faulting of the 1954 Fairview Peak (M_S 7.2) and Dixie Valley (M_S 6.8) earthquakes, Central Nevada, *Bull. Seismol. Soc. Am.* **86,** 761–787.

Convers, J. A., and A. V. Newman (2011). Global evaluation of large earthquake energy from 1997 through mid-2010, *J. Geophys. Res.* **116,** no. B08304, doi: 10.1029/2010JB007928.

Dickinson, H., A. M. Freed, and C. Andronicos (2016). Inference of the viscosity structure and mantle conditions beneath the Central Nevada seismic belt from combined postseismic and lake unloading studies, *Geochem., Geophys., Geosys.* **17,** no. 5, 1740–1757, doi: 10.1002/2015GC006207.

Dickinson, W. R. (2006). Geotectonic evolution of the Great Basin, *Geosphere* **2,** 535–368, doi: 10.1130/GES00054.1.

Dixon, T. H., M. Miller, F. Farina, H. Wang, and D. Johnson (2000). Present-day motion of the Sierra Nevada block and some tectonic implications for the Basin and Range province, North American Cordillera, *Tectonics* **19,** 1–24, doi: 10.1029/1998TC001088.

Elliott, A. J., S. Dee, R. D. Koehler, W. D. Barnhart, R. Briggs, C. Collett, T. Dawson, S. DeLong, R. D. Gold, E. K. Haddon, *et al.* (2020). Comparison of ground-based and space-based surface rupture mapping of the May 15, 2020 M 6.5 Monte Cristo Range Earthquake, Nevada, *Poster Presented 107 at 2020 SCEC Annual Meeting*, SCEC Contribution Number 10489, Poster Number 107, Poster Presented 107 online from 14–17 September 2020.

Faulds, J. E., C. D. Henry, and N. H. Hinz (2005). Kinematics of the northern Walker Lane: An incipient transform fault along the Pacific-North American plate boundary, *Geology* **33,** 505–508, doi: 10.1130/G21274.1.

Hammond, W. C., and W. Thatcher (2007). Crustal deformation across the Sierra Nevada, northern Walker Lane, Basin and Range transition, western United States measured with GPS, 2000–2004, *J. Geophys. Res.* **112,** no. B5, doi: 10.1029/2006JB004625.

Hammond, W. C., G. Blewitt, C. Kreemer, R. D. Koehler, and S. Dee (2021). Geodetic observation of seismic cycles before, during, and after the 2020 Monte Cristo Range, Nevada earthquake, *Seismol. Soc. Am.* **92,** no. 2A, 647–662.

Ji, C., D. V. Helmberger, D. J. Wald, and K. F. Ma (2003). Slip history and dynamic implications of the 1999 Chi-Chi, Taiwan, earthquake, *J. Geophys. Res.* **108,** no. B9, doi: 10.1029/2002JB001764.

Ji, C., D. J. Wald, and D. V. Helmberger (2002). Source description of the 1999 Hector Mine, California, earthquake, part I: Wavelet domain inversion theory and resolution analysis, *Bull. Seismol. Soc. Am.* **92,** no. 4, 1192–1207, doi: 10.1785/0120000916.

Jin, Z., and Y. Fialko (2020). Finite slip models of the 2019 Ridgecrest earthquake sequence constrained by space geodetic data and aftershock locations, *Bull. Seismol. Soc. Am.* **110,** no. 4, 1660–1679, doi: 10.1785/0120200060.

Koehler, R. D., S. Dee, A. Elliott, A. Hatem, A. Pickering, I. Pierce, and G. Seitz (2021). Field response and surface-rupture characteristics of the 2020 M 6.5 Monte Cristo Range Earthquake, Central Walker Lane, Nevada, *Seismol. Soc. Am.* **92,** no. 2A, 823–839.

Liu, C., T. Lay, E. E. Brodsky, K. Dascher-Cousineau, and X. Xiong (2019). Coseismic rupture process of the large 2019 Ridgecrest earthquakes from joint inversion of geodetic and seismological observations, *Geophys. Res. Lett.* **46,** 11,820–11,829, doi: 10.1029/2019GL084949.

Liu, C., T. Lay, Z. Xie, and X. Xiong (2019). Intraslab deformation in the 30 November 2018 Anchorage, Alaska, MW 7.1 earthquake, *Geophys. Res. Lett.* **46,** no. 5, 2449–2457, doi: 10.1029/2019GL082041.

Mangino, S. G., G. Zandt, and C. J. Ammon (1993). The receiver structure beneath Mina, Nevada, *Bull. Seismol. Soc. Am.* **83,** no. 2, 542–560.

Nagorsen-Rinke, S., J. Leee, and A. Calvert (2013). Pliocene sinistral slip across the Adobe Hills, eastern California-western Nevada: Kinematics of faul slip transfer across the Mina deflection, *Geosphere* **9,** 37–53, doi: 10.1130/GES00825.1.

Putirka, K. D., and C. J. Busby (2011). Introduction: Origin and evolution of the Sierra Nevada and Walker Lane, *Geosphere* **7,** 1269–1272, doi: 10.1130/GES0076.1.

Ruhl, C. J., E. A. Morton, J. M. Bormann, R. Hatch-Ibarra, G. Ichinose, and K. D. Smith (2021). Complex fault geometry of the 2020 Mww 6.5 Monte Cristo Range, Nevada, earthquake sequence, *Seismol. Soc. Am.* **92,** no. 3, 1876–10.

Sandwell, D., R. Mellors, X. Tong, X. Xu, M. Wei, and P. Wessel (2016). GMTSAR: An InSAR processing system based on generic mapping tools, Second Ed., 1–120.

Socquet, A., J. Hollingsworth, E. Pathier, and M. Bouchon (2019). Evidence of supershear during the 2018 magnitude 7.5 Palu earthquake from space geodesy, *Nature Geosci.* **12,** no. 3, 192–199, doi: 10.1038/s41561-018-0296-0.

Thatcher, W., G. R. Foulger, B. R. Julian, J. L. Svarc, E. Quilty, and G. W. Bawden (1999). President-day deformation across the Basin and Range province, western United States, *Science* **283,** 1714–1718, doi: 10.1126/science.283.5408.1714.

Wessel, P., and W. H. Smith (1991). Free Celps map and display data, *Eos Trans. AGU* **72,** no. 41, 441–446, doi: 10.1029/90EO00319.

Xu, J., C. Liu, and X. Xiong (2020). Source process of the 24 January 2020 Mw 6.7 East Anatolian fault zone, Turkey, earthquake, *Seismol. Soc. Am.* **91,** no. 6, 3120–3128.

Yano, T. E., G. Shao, Q. Liu, C. Ji, and R. J. Archuleta (2014). Coseismic and potential early afterslip distribution of the 2009 Mw 6.3 L'Aquila, Italy earthquake, *Geophys. J. Int.* **199,** no. 1, 23–40, doi: 10.1093/gji/ggu241.

Zhang, G., X. Shan, B. Delouis, C. Qu, J. Balestra, Z. Li, Y. Liu, and G. Zhang (2013). Rupture history of the 2010 Ms 7.1 Yushu earthquake by joint inversion of teleseismic data and InSAR measurements, *Tectonophysics* **584,** 129–137, doi: 10.1016/j.tecto.2012.03.024.

Zheng, A., X. Chen, and W. Xu (2020). Present-day deformation mechanism of the northeastern Mina deflection revealed by the 2020 Mw 6.5 Monte Cristo Range Earthquake, *Geophys. Res. Lett.* **47,** no. 22, e2020GL090142, doi: 10.1029/2020GL090142.

Manuscript received 16 October 2020
Published online 13 July 2021

Supporting Online Material for

Seismic and geodetic analysis of rupture characteristics of the 2020 M_W 6.5 Monte Cristo Range, Nevada earthquake

Chengli Liu[1], Thorne Lay[2], Fred F. Pollitz[3], Jiao Xu[4] and Xiong Xiong[1]

1. Institute of Geophysics and Geomatics, China University of Geosciences, Wuhan, China.
2. Department of Earth and Planetary Sciences, University of California, Santa Cruz, CA, USA.
3. U.S. Geological Survey, Moffett Field, California, USA.
4. College of Geomatics and Geoinformation, Guilin University of Technology, Guilin, China.

Corresponding author: liuchengli@cug.edu.cn

This file includes:

InSAR data processing

We selected the ascending and descending TOPSAR mode radar images acquired by the C-band Sentinel-1A/B satellites (Table S2) to calculate the surface deformation for the 2020 Nevada earthquake. We used the open source GMTSAR software (Sandwell et al., 2016) to process the single look complex images. The image pairs were processed following these steps: image co-registration, generating topographic phase, and performing interferometry. Then the 90 m resolution Shuttle Radar Topography Mission digital elevation model was adopted to remove topographic phase from the interferograms. The program SNAPHU, which is based on a minimum cost flow algorithm, was used to unwrap the interferograms (Chen and Zebker, 2002). We detrend the InSAR deformation map by fitting a plane using the displacement areas that were not affected by the coseismic deformation to reduce the orbital and possible ionospheric errors. The interferograms and the line-of-sight (LOS) displacement from ascending and descending tracks are shown in Figure S12 and Figure 3, respectively. For efficient inversion, we resampled the LOS displacements to less than 500 points from each interferogram using a quadtree algorithm (Lohman and Simons, 2005).

References

Chen, C. W., & Zebker, H. A. (2002). Phase unwrapping for large SAR interferograms: Statistical segmentation and generalized network models. *IEEE Transactions on Geoscience and Remote Sensing*, 40(8), 1709-1719.

Hammond, W. C., & Thatcher, W. (2007). Crustal deformation across the Sierra Nevada, northern Walker Lane, Basin and Range transition, western United States measured with GPS, 2000–2004. *Journal of Geophysical Research: Solid Earth*, 112(B5).

Lohman, R. B., & Simons, M. (2005). Some thoughts on the use of InSAR data to constrain models of surface deformation: Noise structure and data downsampling. *Geochemistry, Geophysics, Geosystems*, 6(1).

Sandwell, D., Mellors, R., Tong, X., Xu, X., Wei, M., & Wessel, P. (2016). GMTSAR: An

InSAR Processing System Based on Generic Mapping Tools (Second Edition), 1–120.

Ji, C., Wald, D. J., & Helmberger, D. V. (2002). Source description of the 1999 Hector Mine, California, earthquake, part I: Wavelet domain inversion theory and resolution analysis. *Bulletin of the Seismological Society of America*, 92(4), 1192-1207.

Figures

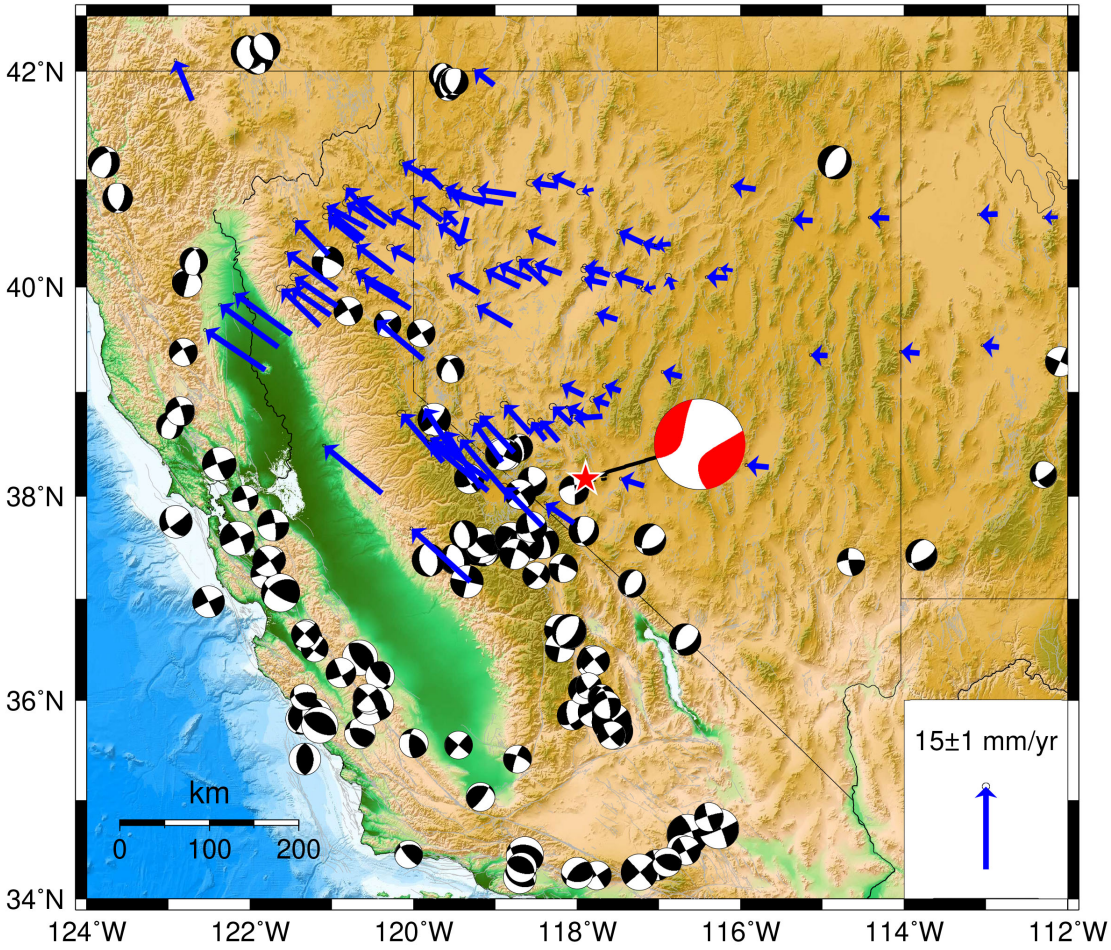

Figure S1. The blue arrows show the regional GPS Velocities with respect to stable North America (Hammond & Thatcher, 2007). Best double-couple solutions ($M \geq 6.0$) of the gCMT catalog from 1976 to 2020 preceding the M_W 6.5 Nevada earthquake are shown in black. The W-phase focal mechanism of the 2020 Nevada mainshock is shown with red and the red star locates the epicenter.

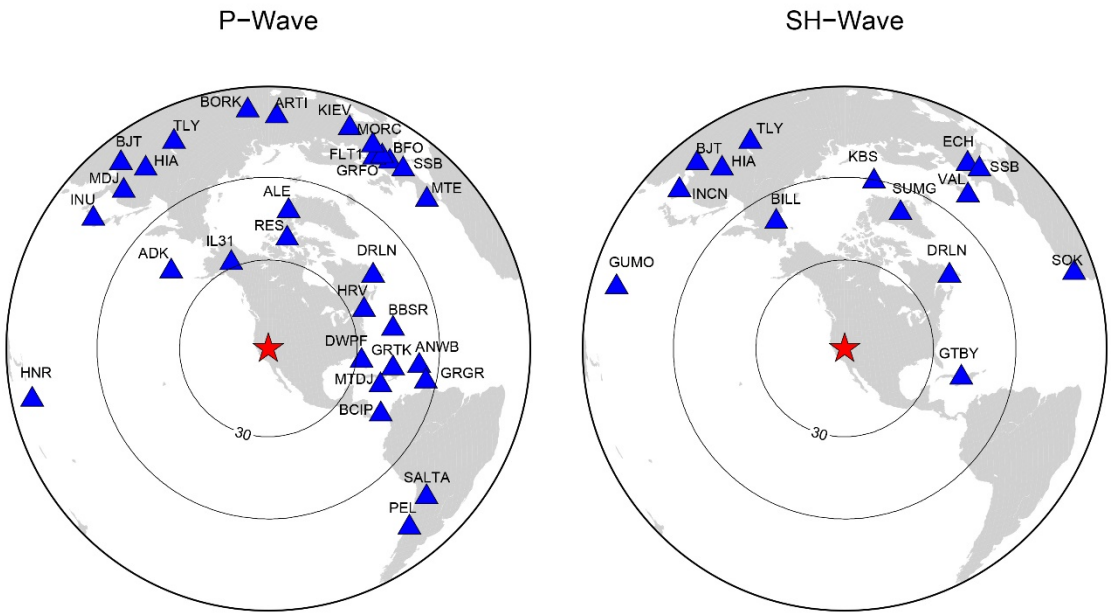

Figure S2. The distributions of teleseismic broadband seismic stations providing P (left) and SH (right) observations used in the joint inversion.

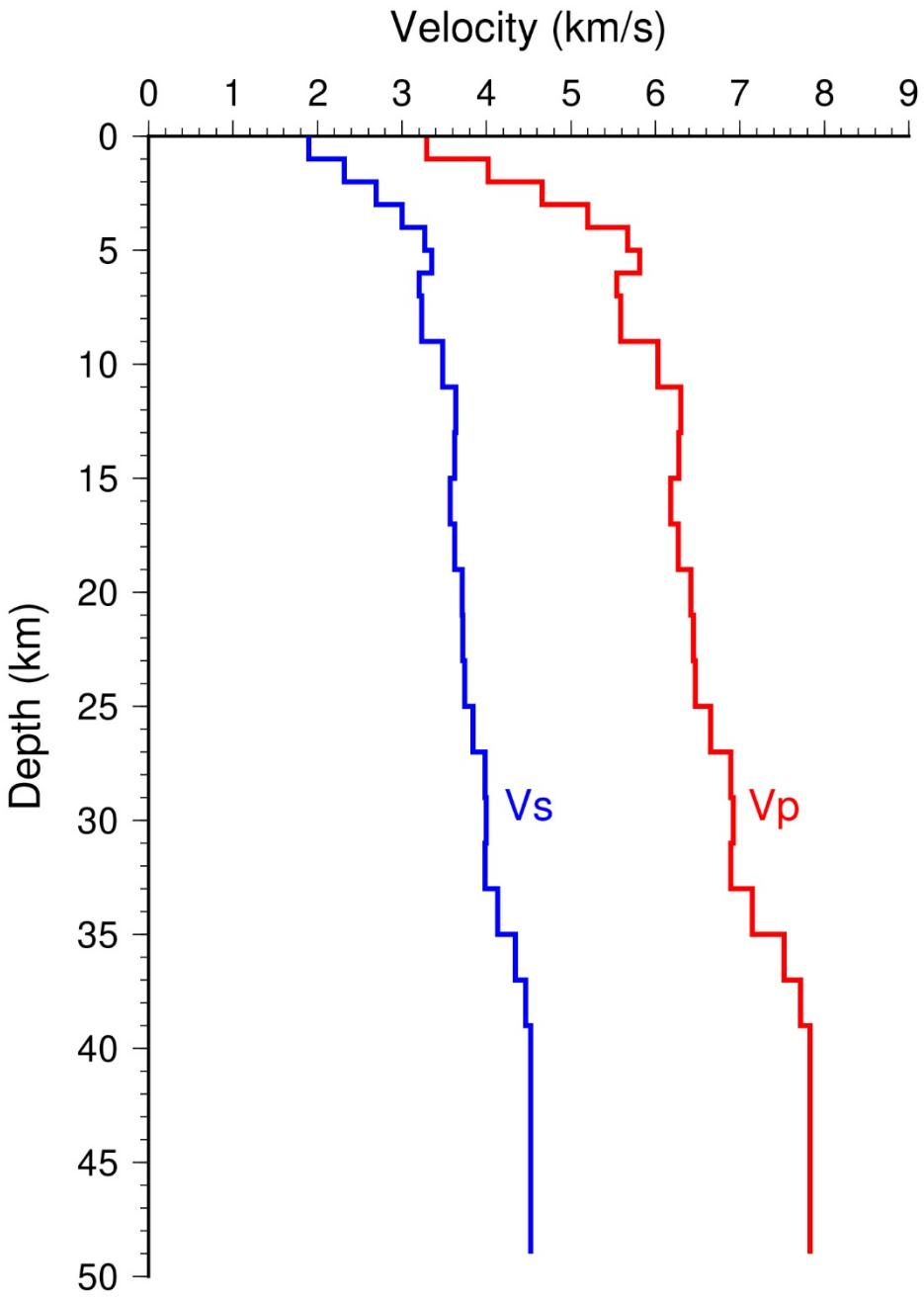

Figure S3. Regional 1D velocity model of Mangino et al. (1993) used in this study.

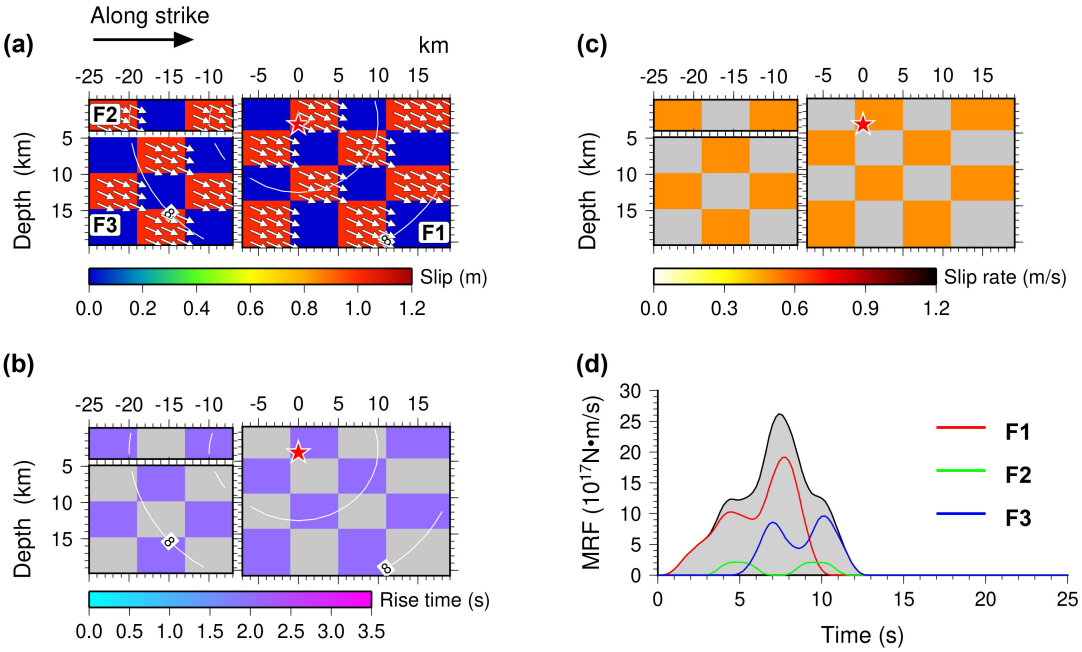

Figure S4. Checkerboard test for different parameters. (a) Input model with 1.0 m slip assigned to every other 6 km × 4.95 km region (3 x 3 subfault patches) (b) and (c) are the corresponding rise time (2.0 s) and slip rate of the input model (0.5 m/s), respectively. (d) The moment rate function for each input fault segment.

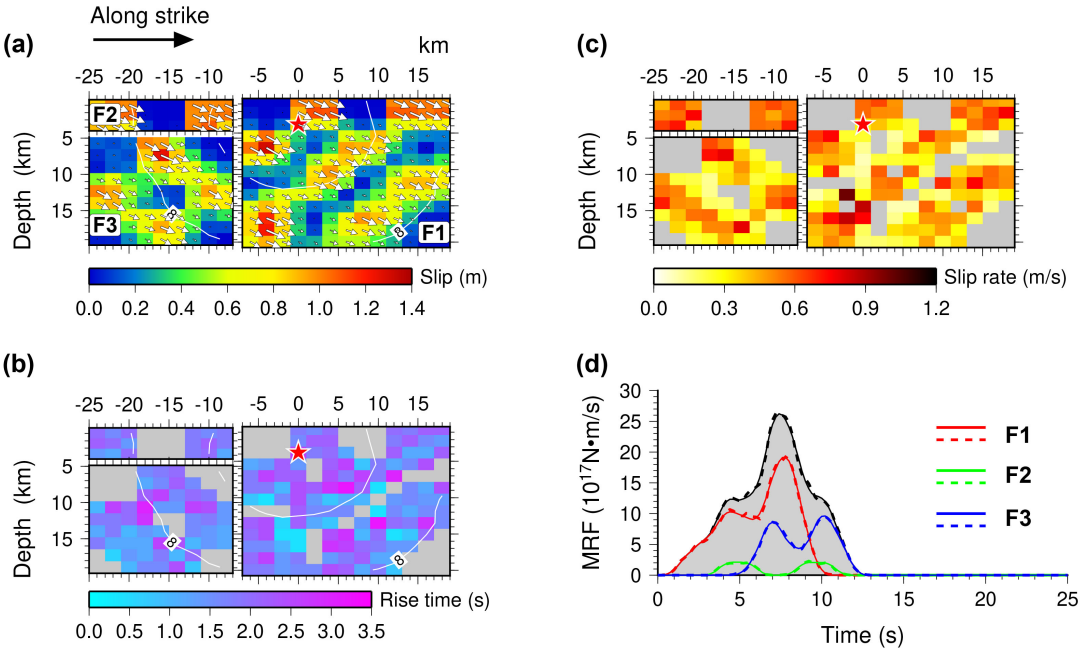

Figure S5. The checkerboard model (Figure S4) inversion slip model from joint inversion of the synthetic datasets.

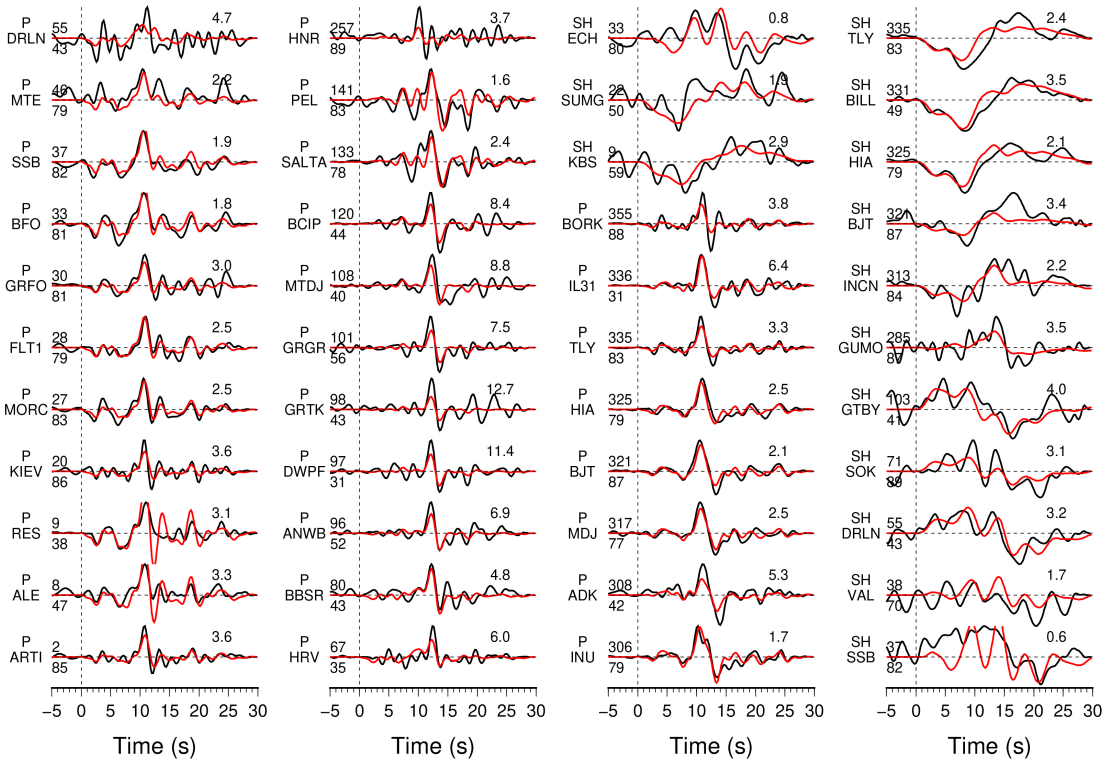

Figure S6. Comparison of observed (black) and synthetic (red) teleseismic *P* and *SH* wave ground velocities for the preferred slip model in Figure 5 with three fault segments. Data and synthetic seismograms are manually aligned on the first arrivals. Station names and phase type are indicated on the left of each comparison. The number above the right portion of each comparison is the peak amplitude of the observed ground displacement in μm/s. The azimuth (above) and distance (below) in degrees are shown at the beginning of each record.

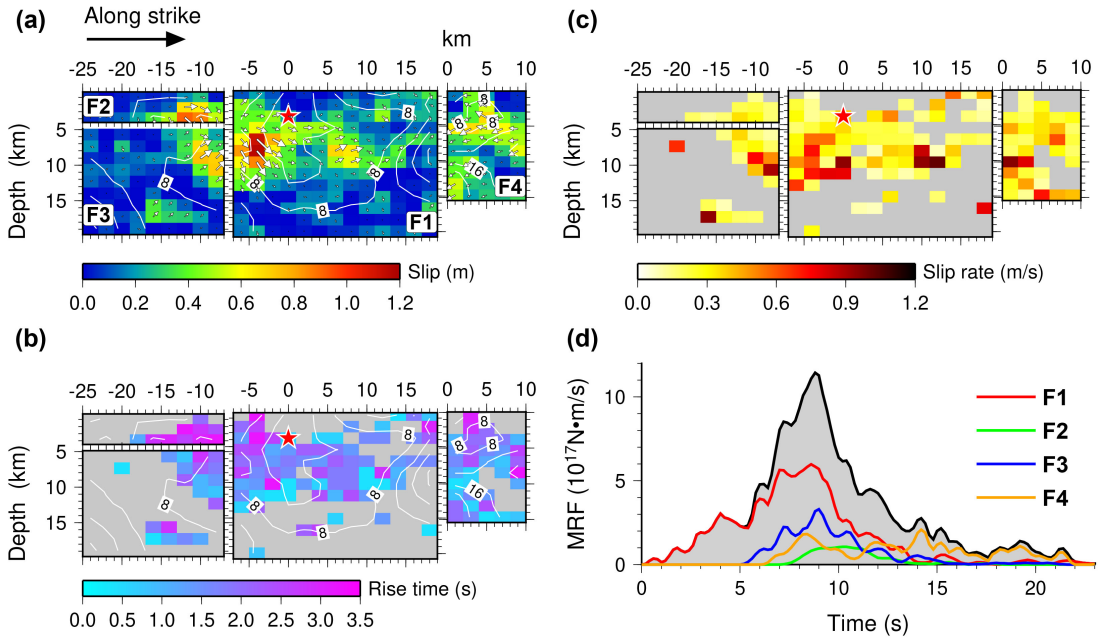

Figure S7. The inverted four-fault slip distribution by joint inversion using GNSS, InSAR and seismic waveforms. (a) The inverted slip distribution on four fault segments, for which the fault parameters are listed in Table S2. The red star locates the hypocenter on F1. White contours indicate the rupture initiation time in seconds. White arrows indicate the direction and amplitude of slip of the hanging wall relative to the footwall.. The color bar shows the slip amplitude scale. (b) and (c) are the distribution of rise time and slip rate of the rupture model, respectively; subfaults with slip magnitude less than 0.2 m are excluded. (d) The moment rate function for the slip model. Contributions from the four fault segments are shown by colored curves and the gray-shaded region indicates the total moment rate.

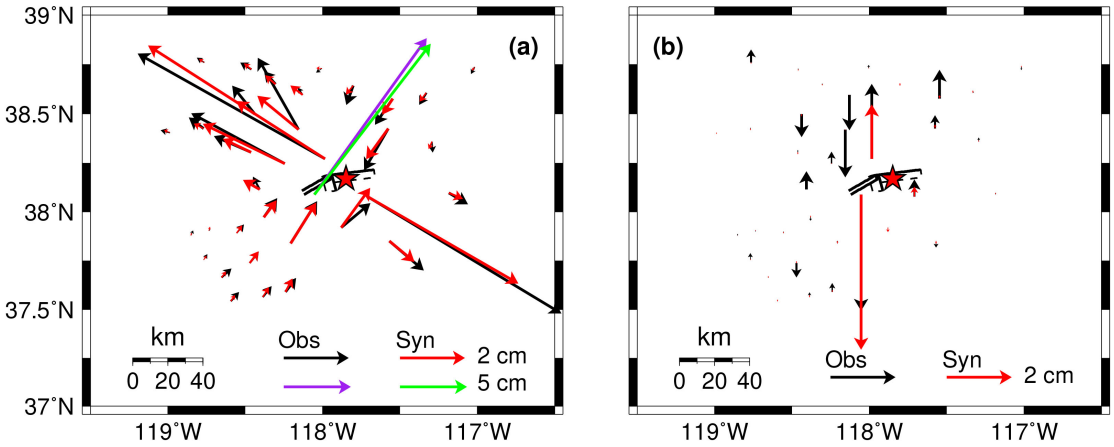

Figure S8. Comparison between the observed and synthetic GNSS coseismic displacements of the 2020 Nevada earthquake for the four-fault finite-fault inversion in Figure S7. (a) The data (black and purple) and synthetic (red and green) horizontal GNSS components. (b) The vertical GNSS component data (black) and synthetics (red). The black rectangles indicate the assumed fault model with the shallow (surface) edge having a solid line.

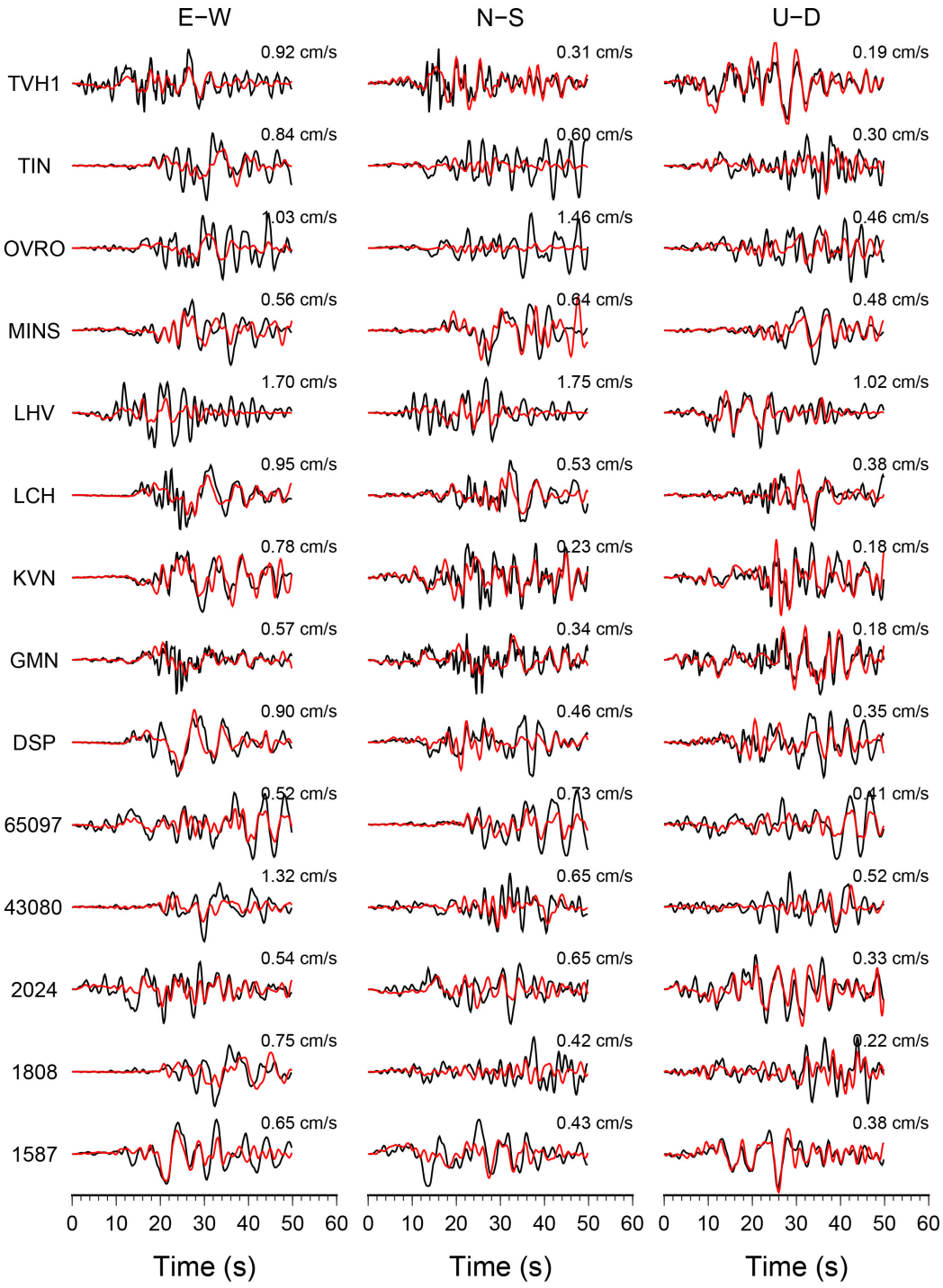

Figure S9. Comparison of the observed three-component strong-motion records (black lines) and synthetic seismograms (red lines) for the four-fault joint slip model in Figure S7. Both data and synthetics are manually aligned on the first P arrivals and band pass filtered between 0.02 Hz and 0.625 Hz. The station name is indicated on the left; the number at the top right of each trace is the maximum velocity of the observed signals in cm/s.

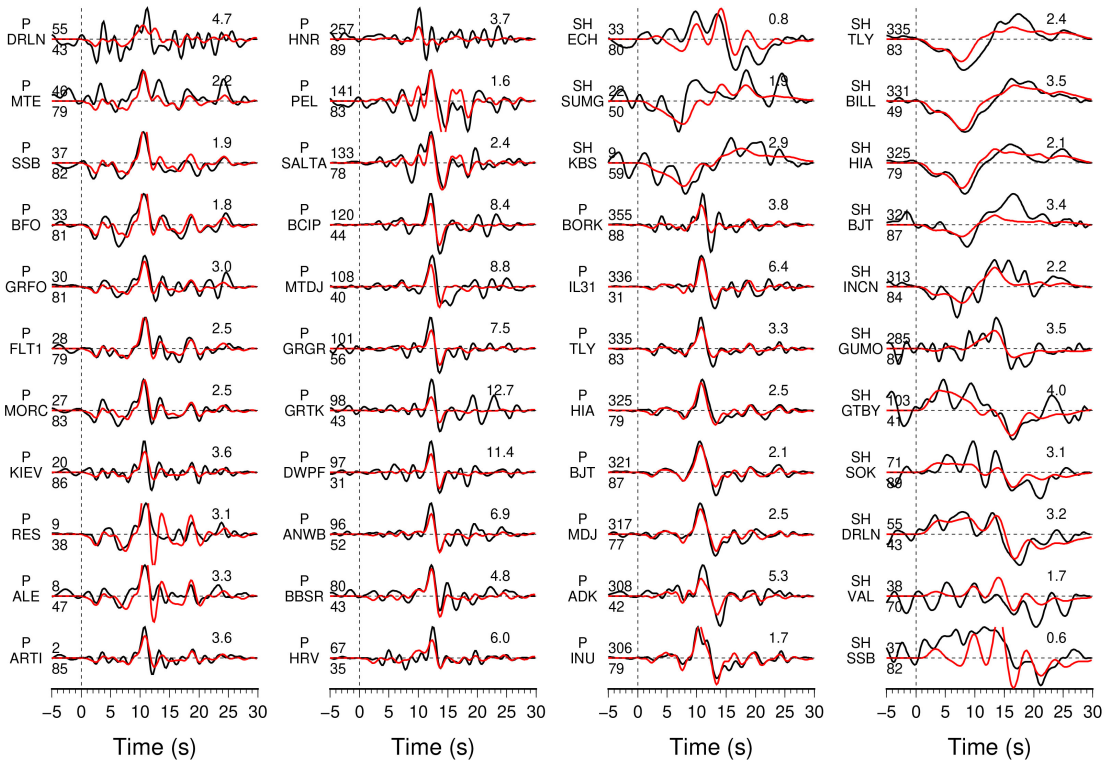

Figure S10. Comparison of observed (black) and synthetic (red) teleseismic P and SH wave ground velocities for the joint slip model in Figure S7. Data and synthetic seismograms are manually aligned on the first arrivals. Station names and phase type are indicated on the left of each comparison. The number above the right portion of each comparison is the peak amplitude of the observed ground displacement in μm/s. The azimuth (above) and distance (below) in degrees are shown at the beginning of each record.

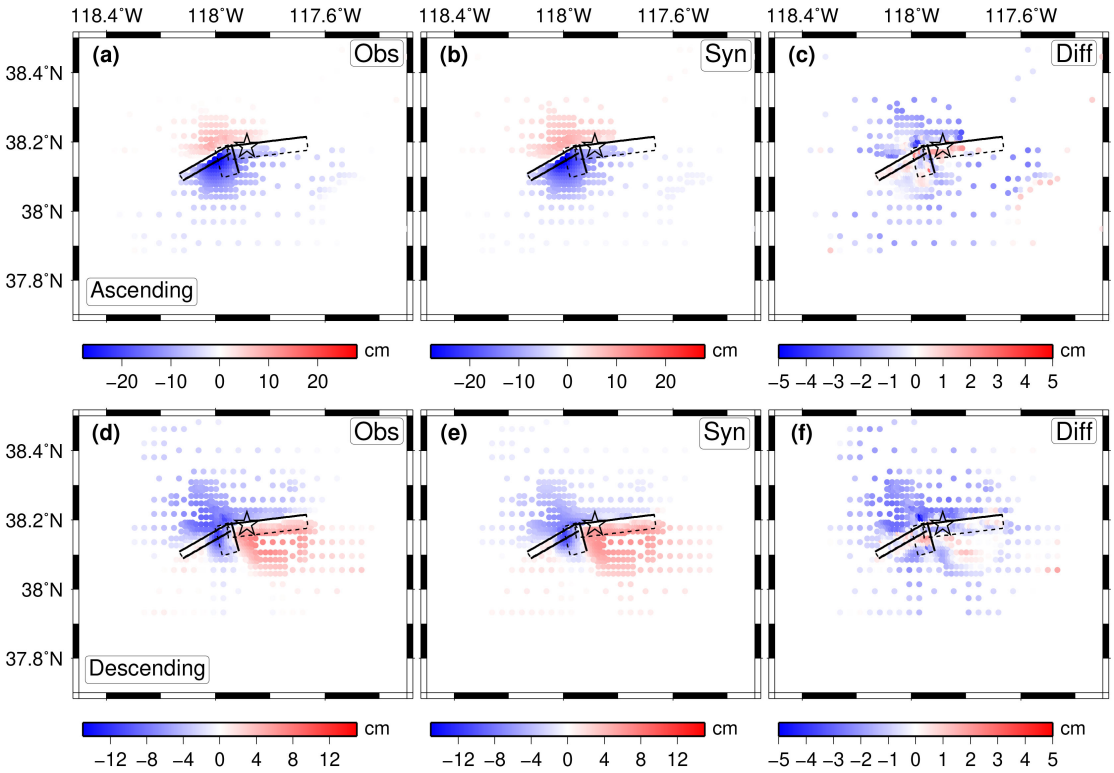

Figure S11. Line-of-sight (LOS) displacement fields and synthetics. (a) and (d) LOS displacements for the ascending and descending Sentinel-1, respectively. (b) and (e) Synthetic LOS displacements from the four-fault joint inversion model in Figure S7. (c) and (f) Residuals of LOS displacements along the ascending and descending path, respectively. Note the difference in color scale. The rectangles show the fault plane, and the star is the epicenter of the mainshock. The black solid and dashed outlined rectangles indicate the fault segments used in the joint inversion, with the solid side at the shallow edge.

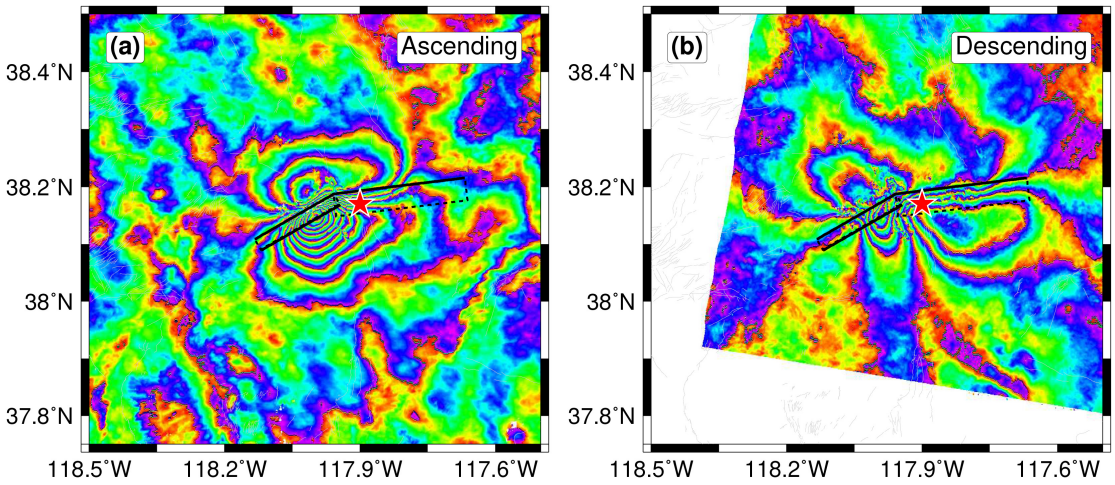

Figure S12. Wrapped InSAR observations of the M_W 6.5 Nevada earthquake. (a) and (b) show interferograms field of the ascending and descending paths, respectively. The black solid and dashed outlined rectangles indicate the fault segments used in the joint inversion, with the solid side at the shallow edge.

Table S1. Coseismic displacements of the Monte Cristo Range earthquake used in this study (Hammond et al., 2021).

StationID	Lontitude	Latitude	East(mm)	North(mm)	UP(mm)
COLU	-118.054	38.089	83.83	116.69	-35.73
ARMY	-118.438	38.498	-7	8.78	-7.06
CALA	-118.129	38.596	-1.44	2.2	-10.93
CHIA	-118.207	37.838	8.14	13	0.84
DRYC	-117.33	38.607	-2.24	-3.7	0.47
EPAS	-117.881	37.92	9.02	7.55	-0.2
FLAT	-118.463	38.304	-11.47	4.99	0.73
INDI	-118.304	38.65	-3.53	3.99	0
INKH	-117.017	38.736	-1.11	-2.13	-0.94
JACK	-118.406	38.114	-2.07	3.93	5.66
LUCK	-118.769	38.424	-4.53	3.4	0.33
MINA	-118.155	38.42	-12.55	22.11	-14.72
MOHO	-118.245	38.246	-28.78	15.49	3.66
MONT	-117.708	38.078	59.68	-35.98	5.24
P132	-118.005	38.729	-1.76	-1.29	1.03
P133	-118.46	38.725	-3.39	2.07	0.34
P627	-118.379	37.973	4.09	5.86	-1.05
P641	-118.852	37.878	0.67	1.5	0.54
P645	-118.594	37.541	2.54	2.83	0.43
P647	-118.768	37.754	1.14	1.77	2.11
P649	-118.736	37.904	0.46	0.42	-0.3
P650	-118.555	37.891	2.27	2.68	0.53
P651	-118.387	37.563	2.73	3.37	1.52
P652	-118.239	37.589	3.29	4.33	2.78
P653	-118.472	37.738	2.75	3.43	-4.41
PACT	-117.803	38.642	-2.12	-5.96	0.39
PILO	-117.985	38.27	-57.64	32.38	23.12
RHIL	-117.575	38.425	-7.45	-12.81	4.18
ROJO	-117.546	38.577	-5.46	-8.01	8.91
ROUG	-118.987	38.403	-2.87	0.76	-0.28
TONI	-117.293	38.358	0.23	-3.34	1.28
TONO	-117.184	38.097	5.94	-3.54	-0.49
WALK	-118.764	38.759	-2.32	1.5	4
WATC	-118.654	37.664	3.04	2.74	-0.08
WEEP	-117.569	37.85	10.61	-9.07	-1.99

Table S2. The Sentinel-1A/B acquisitions used for Interferometric Synthetic Aperture Radar (InSAR) in this study.

Track	reference image	secondary image	Perp. B	Inclined Angle	Azimuth
	(yyyy/mm/dd)	(yyyy/mm/dd)	(m)	(°)	(°)
64(A)	2020/05/11	2020/05/17	20	35-47	-10
71(D)	2020/05/11	2020/05/17	19	35-47	-170
Perp. B is the perpendicular baseline; A and D denotes ascending and descending, respectively.					

Table S3. Fault parameters used in the joint inversion.

	Fault segments			
	F1	F2	F3	F4
Strike	83°	60°	60°	165°
Dip	78°	60°	90°	60°

Table S4. The misfit of the various dataset for the three-fault model.

Data set	Misfit
Teleseismic	0.291
Strong-motion	0.302
GNSS	0.447
InSAR	9.885

The calculations of the waveform and statics misfit are defined by Ji et al., 2002.